International Journal of Solids and Structures 49 (2012) 3367–3380

Contents lists available at SciVerse ScienceDirect

International Journal of Solids and Structures

journal homepage: www.elsevier.com/locate/ijsolstr

Two-phase damage modeling of concrete affected by alkali–silica reaction under variable temperature and humidity conditions

Claudia Comi *, Beatrice Kirchmayr, Rossella Pignatelli

Department of Structural Engineering, Politecnico di Milano, Piazza L. da Vinci 32, 20133 Milan, Italy

ARTICLE INFO

Article history:
Received 6 December 2011
Received in revised form 30 June 2012
Available online 31 July 2012

Keywords:
Concrete
ASR
Damage
Humidity

ABSTRACT

In the present work the concrete affected by alkali–silica reaction (ASR) is represented as a two-phase material made of a solid skeleton and a wet expanding gel, which exerts a pressure capable of severely damaging the concrete surrounding the reactive sites. Both the effects of temperature and humidity conditions on the kinetic of the chemical reaction and on the final value of the consequent expansion are included in the proposed model. The mechanical degradation induced by the ASR is described by a phenomenological isotropic damage model. The constitutive model, implemented in a finite element code, is used for the analyses of structures made of reactive concrete in the presence of temperature and moisture gradients. Firstly the temperature and humidity fields are obtained through uncoupled heat and moisture transport analyses and then the chemo-mechanical analysis is performed starting from the values of temperature and humidity preliminary calculated.

1. Introduction

Alkali silica reaction (ASR) is one of the chemical reactions affecting the concrete durability. During ASR certain forms of silica in aggregates react with the high alkaline solution in concrete micro pores to form a hydrous alkali-calcium-silica gel that expands in the presence of moisture and causes slow but severe deterioration of concrete structures.

The presence of the alkali–silicate gel is not damaging to the concrete per se, since the gel initially fills up the pre-existing concrete pores. However, in time the volume expansion of this gel may generate significant internal tensile stresses in the concrete skeleton, sufficient to crack both the affected aggregate and surrounding cement paste.

At the macro-scale ASR typically manifests itself through extensive surface map cracking, although restraints due to structural loading or reinforcements may modify the observed cracking pattern. The progress of the reaction can be extremely slow, and signs of degradation may only appear when the concrete structure is years to decades old. The tensile strength and elastic modulus of the concrete can be severely compromised as the reaction develops, while compressive strength is usually little affected.

Water plays a major role in the degradation of structures affected by ASR. Experimental studies reported by Gudmundsson and Asgeirsson (1983), Larive (1998), Multon (2003) and Ahmed et al. (2003) show that the presence of water during ASR-products formation increases the final concrete expansion while after completion of the chemical reactions, any added water does not cause extra swelling. Others experimental campaigns (Larive, 1998; Multon, 2003; Chatterji and Christensen, 1990) evidence that the temperature is another key factor influencing the reaction kinetics and in particular show that a higher temperature induces a faster reaction.

In parallel with the experimental studies, several mathematical models have been proposed in the literature to simulate the mechanical effects of ASR. In early proposed models (e.g. Charlwood (1994)) an equivalent inelastic strain was defined to reproduce the overall structural expansion. Subsequently, more refined models have been proposed (Léger et al., 1996; Saouma and Perotti, 2006), with focus on the kinetics of the reaction. In Saouma and Perotti (2006) the kinetics law, based on Larive's proposal, also includes, in a heuristic way, the effect of the stress state. Other models address the mechanical modeling of ASR by considering a two-phase material with the concrete skeleton and the expansive gel acting in parallel (Ulm et al., 2000; Farage et al., 2004; Fairbairn et al., 2006). Ulm et al. (2000) consider an elasto-plastic behavior for concrete, while Farage et al. (2004) and Fairbairn et al. (2006) use a smeared crack approach to take into account anisotropy.

These works focus on the thermo-activation of ASR but neglect the influence of the moisture on the advancement and on the final extent of the reaction. In spite of some recent campaigns focused on the comprehension of the influence of moisture on ASR (e.g. Poyet, 2003; Poyet et al., 2006), still very few attempts have been done to model the dependence of ASR on temperature and

* Corresponding author. Tel.: +39 02 2399 4215; fax: +39 02 2399 4220.
E-mail addresses: comi@stru.polimi.it, claudia.comi@polimi.it (C. Comi), maria.kirchmayr@mail.polimi.it (B. Kirchmayr), pignatelli@stru.polimi.it (R. Pignatelli).

0020-7683/$ - see front matter © 2012 Elsevier Ltd. All rights reserved.
http://dx.doi.org/10.1016/j.ijsolstr.2012.07.015

moisture simultaneously. An exception is represented by Saouma et al. (2007), who introduce the dependence by humidity through a simple function multiplying the asymptotic strain and the reaction rate, and by Grimal et al. (2008), who introduce the influence of both temperature and moisture in the kinetic law of the reaction and give a complete model for the behavior of the reactive concrete, considering the concrete creep, the stress induced by the formation of ASR gel and the mechanical damage.

In the present work the phenomenological bi-phase isotropic damage model accounting for the effect of varying temperature conditions proposed in Comi et al. (2009) is extended in order to catch the structural effects induced by the alkali–silica reaction in concrete structures when also ambient humidity conditions change and moisture gradients occur. As in Comi and Pignatelli (2010) the quantity of water present in the structure is taken into account through the degree of saturation of concrete and, in the framework of Biot's theory of multi-phase porous materials, concrete is here conceived as a two-phase material constituted by the superposition of two homogenized phases: the concrete skeleton and the wet gel produced by the chemical reaction, which in turns is constituted by the dry gel, the liquid water and the vapor.

As firstly proposed by Larive (1998), the ASR kinetic is assumed to be stress independent and is described by using an intrinsic time, expressed as a function of both the latency time and the characteristic time. In this work these times depend on both temperature and degree of saturation. The ASR kinetics here proposed is an enhancement of the one introduced by the Authors in Comi and Pignatelli (2011).

When the external humidity boundary conditions are not homogeneous, the moisture gradients are taken into account through a diffusion analysis of moisture in its liquid form, while varying temperature conditions requires a heat diffusion analysis. The different role of moisture and temperature in slender and massive structures affected by ASR can be justified by the proposed model considering that the two diffusion mechanisms introduce two characteristic lengths, numerically very different for concrete.

In order to assess the decrease of stiffness of the concrete due to cracking caused by ASR, the response of the homogenized concrete skeleton is described by a suitably adapted version of a "bi-dissipative" damage model for concrete, previously developed by Comi and Perego (2001).

The proposed model is first calibrated on the basis of experimental data provided by accelerated laboratory tests, documented in the literature (Larive, 1998; Multon, 2003; Multon and Toutlemonde, 2006). Then, the model is validated by simulating the structural tests performed by Multon and Toutlemonde (2010) on plain and reinforced reactive concrete beams subject to varying moisture condition at constant temperature. As a second example, the mechanical response of the Beauharnois gravity dam affected by ARS is computed and qualitatively compared with the actual data on macro crack appearance and crest displacements reported in Bérubé et al. (2000) and Kladek et al. (1995). Since the local evolution of ASR swelling is governed by both temperature and humidity, the steady-harmonic temperature and degree of saturation fields within the dam are computed preliminarily. In doing so, the mechanical analysis with the proposed damage model is assumed to be coupled only in one direction with the previous heat and moisture-diffusion problems.

2. Chemo-damage model

2.1. Two-phase model

In the framework of Biot's theory of multi-phase porous materials (Coussy, 2004), concrete affected by ASR is conceived as a two-phase heterogeneous material constituted by the homogenized concrete skeleton (s), that includes the cement paste, the aggregates and the non-connected porosity, and the homogenized wet gel (gw), combination of the gel produced by the chemical reaction, the adsorbed water and the gas phases (aqueous vapor and dry air).

Let V be the total volume of the representative volume element RVE, V_s the volume occupied by the solid and $V_{gw} = V_g + V_w + V_v$ the volume occupied by the wet gel, which includes the dry gel of volume V_g, the liquid water of volume V_w and the vapor phases of volume V_v (see Fig. 1). The degree of saturation for the water is defined as $S_w = V_w/(V - V_s - V_g)$. The total porosity $\phi = (V - V_s)/V$ is filled by the dry gel, the liquid water and the gas. One can also introduce the water porosity as the portion of the total porosity filled by water and gas $\phi_w = (V - V_s - V_g)/V$. With these definitions, the volumetric fraction of the wet gel can be expressed as

$$\zeta_{gw} = V_{gw}/V \tag{1}$$

The bi-phase modeling, instead of a three-phase modeling (see e.g. Grimal et al. (2008)and Comi and Pignatelli (2011)), is justified by the different permeability of concrete with respect to water and gel. Namely, concrete is much more permeable to the water than to the gel, hence one can assume locally drained conditions with respect to water (so that water pressure can be neglected) and locally undrained condition for the gel transport. The representative volume can exchange water with the surrounding medium, while no gel migration is allowed.

2.2. Field equations

Assuming small strains and quasi-static conditions the compatibility and equilibrium for the multi-phase solid read

$$\boldsymbol{\varepsilon} = \frac{1}{2}\left(grad\mathbf{u} + grad^T\mathbf{u}\right) \tag{2}$$

$$div\boldsymbol{\sigma} + \rho\mathbf{b} = \mathbf{0} \tag{3}$$

where $\mathbf{u}$ is the skeleton displacement, $\boldsymbol{\varepsilon}$ is the tensor of small strain of the skeleton, $\boldsymbol{\sigma}$ is the Cauchy stress in the combined solid and fluid mix, ρ is the density of the assembly and $\rho\,\mathbf{b}$ is the body force of the solid and the fluid mix.

The conservation law for the liquid water can be written as

$$div(\rho_w\phi_w S_w\dot{w}_w) + \frac{\partial(\rho_w\phi_w S_w)}{\partial t} = 0 \tag{4}$$

where t is the time, ρ_w is the mass density of water and $\dot{w}_w$ is the relative velocity of water with respect to the solid.

As already remarked, the low permeability of concrete with respect to gel allows to neglect the transport of gel, while the

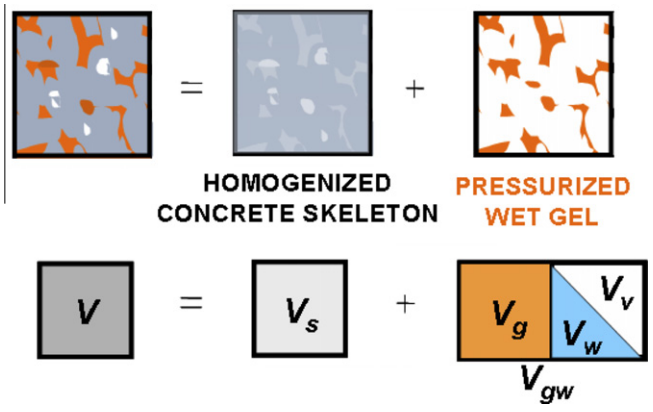

Fig. 1. Schematic representation of the proposed two-phase model.

migration of the water must be described by an appropriate transport law. Here we adopt the simplified equation of moisture transport in its liquid form proposed by Mainguy et al. (2001), valid for slightly porous materials and obtained by the combination of the Darcy's law for fluid flow in porous media with the conservation law (4). The Darcy's law reads:

$$\phi_w S_w \dot{w}_w = -\frac{k}{\eta_w} k_{rw} grad\ p_w \tag{5}$$

where k, η_w, k_{rw} and p_w denote respectively the intrinsic permeability of concrete, the dynamic viscosity, the relative permeability (function of the degree of saturation as in Van Genuchten (1980)) and the pressure of water. In Eq. (5) gravity, inertia or anisotropic effects have been disregarded. Since we are considering atmospheric conditions, the pressure of the gas (vapor and dry air), that is defined relatively to the atmospheric pressure, is null and the water pressure p_w results the opposite of the capillary pressure p_c, whose link with the degree of saturation can be experimentally obtained in the form of the capillary curve. Fig. 2 shows an example of this curve, experimentally obtained from the desoprtion isotherm of concrete specimens, together with the interpolation curve proposed in Baroghel-Bouny et al. (1999). By substituting (5) into the conservation law (4) and taking into account the capillary curve, the following non-linear transport law for moisture in its liquid form is obtained a

$$\phi_w \frac{\partial S_w}{\partial t} + div(D_w grad\ S_w) = 0 \tag{6}$$

where D_w is the permeability of concrete, dependent on the degree of saturation. Using the expression of the capillary curve given in Baroghel-Bouny et al. (1999), the permeability reads

$$D_w(S_w) = m_1 m_2 \left(1 - \frac{1}{m_2}\right) k \frac{\left[1 - (1 - S_w^{1/m_3})^{m_3}\right]^2}{\left[\eta_w S_w^{(1/2+m_2)} (S_w^{-m_2} - 1)^{\frac{1}{m_2}}\right]} \tag{7}$$

with m_1, m_2 and m_3 material parameters. The values of the coefficients in Eqs. (5) and (7) are reported in Table 1.

Instead of the degree of saturation S_w, often the relative humidity h, i.e. the ratio between the pressure of the vapor and the saturated vapor pressure, is used to describe the water content inside concrete and to specify the boundary conditions. As detailed for example in Li et al. (2004)), the relation between the two variables can be obtained by combining the equation describing the capillary curve in Fig. 2 with the so-called Kelvin's equation, which links the capillary pressure to the relative humidity h and the absolute temperature T (K) and reads

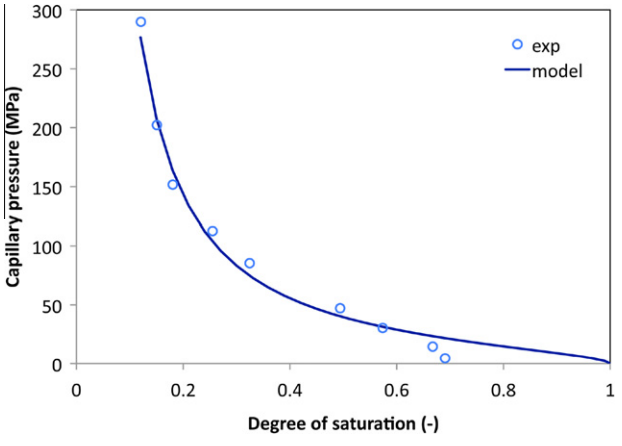

Fig. 2. The experimental capillary curve for concrete (from Baroghel-Bouny et al. (1999)).

Table 1
Elastic parameters and permeability parameters.

Parameter	Value	Unit	Parameter	Value	Unit
E	37300	MPa	η_w	0.01	Pa s
ν	0.22	–	k	$2e^{-21}$	m^2
M	11923	MPa	m_1	37.55	MPa
b	0.41	–	m_2	2.17	–
ϕ_w	0.16	–	m_3	0.46	–

$$\rho_w \frac{RT}{\mathcal{M}_v} \ln h = p_w = -p_c \tag{8}$$

$\mathcal{M}_v$ being the molar mass of vapor. Fig. 3 shows the relation between the degree of saturation and the relative humidity obtained using the capillary curve of Fig. 2 and the Kelvin's equation at $T = 311$ K.

2.3. Constitutive equations

The state equations, relating the static variables (total Cauchy stress $\boldsymbol{\sigma}$, chemical potential $\mu_{gw}$and entropy $\mathcal{S}$) to the conjugate kinematic variables (strain of the skeleton $\boldsymbol{\varepsilon}$, variation of wet gel phase content ζ_{gw} and temperature variation $\theta = T - T_0$, T_0 being the local reference temperature), are derived from the free energy potential Ψ. In order to model the concrete skeleton degradation, we also introduce the internal isotropic damage variable $D = 1 - (1 - D_t)(1 - D_c)$, depending on the two scalar variables D_t and D_c, respectively referred to prevailing tension and compression conditions, and the conjugate energy release rate Y. The following expression for the free energy is proposed:

$$\Psi = \Psi(\boldsymbol{\varepsilon}, \theta, \zeta_{gw}, D) = \frac{(1-D)}{2}\left[2G\mathbf{e} : \mathbf{e} + Ktr^2\boldsymbol{\varepsilon} + Mb^2\left(tr\boldsymbol{\varepsilon} - \frac{\zeta_{gw}}{b}\right)^2 + \left(-\frac{C}{T_0} + M\alpha_{gw}^2\right)\theta^2 - 2Ktr\boldsymbol{\varepsilon}\alpha\theta - 2Mb\left(tr\boldsymbol{\varepsilon} - \frac{\zeta_{gw}}{b}\right)\alpha_{gw}\theta\right] + \psi_{gw}\rho_{gw}\zeta_{gw} \tag{9}$$

In the above equation $\mathbf{e}$ is the deviatoric strain tensor, G and K are respectively the shear and bulk moduli of the homogenized concrete skeleton, M and b are the Biot modulus and the Biot coefficient, C is the volumetric heat capacity, α and α_{gw}, are respectively the volumetric coefficients of thermal expansion for the concrete skeleton and the wet gel. The term $\psi_{gw}\rho_{gw}\zeta_{gw}$ accounts for the free energy supply associated with the mass variation $\rho_{gw}\zeta_{gw}$.

The state equations are obtained by partial derivation and read:

$$\boldsymbol{\sigma} = \frac{\partial \Psi}{\partial \boldsymbol{\varepsilon}} = (1-D)\left\{2G\mathbf{e} + \left[Ktr\boldsymbol{\varepsilon} - K\alpha\theta + Mb\left(btr\boldsymbol{\varepsilon} - \zeta_{gw} - \alpha_{gw}\theta\right)\right]\mathbf{1}\right\} \tag{10}$$

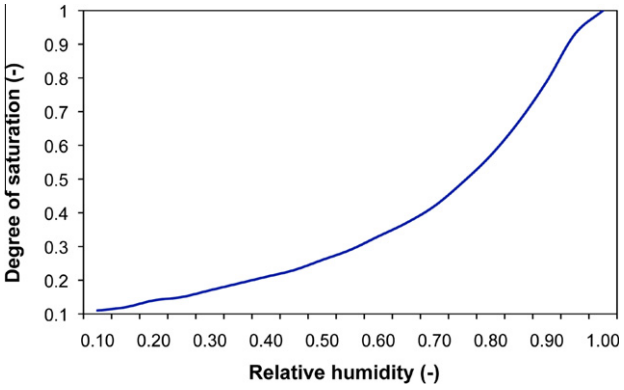

Fig. 3. Relation between degree of saturation and relative humidity for $T = 311$ K.

$$\rho_{gw}\mu_{gw} = \frac{\partial \Psi}{\partial \zeta_{gw}} = -(1-D)M(btr\boldsymbol{\varepsilon} - \zeta_{gw} - \alpha_{gw}\theta) + \rho_{gw}\psi_{gw} \tag{11}$$

$$\mathcal{S} = -\frac{\partial \Psi}{\partial \theta}, Y = -\frac{\partial \Psi}{\partial D} \tag{12}$$

The chemical potential can be expressed in terms of gel pressure p and specific free energy as

$$\mu_{gw} = p/\rho_{gw} + \psi_{gw} \tag{13}$$

By combining (11) and (13) one obtains the following form for the gel pressure

$$p = -(1-D)M\left(btr\boldsymbol{\varepsilon} - \zeta_{gw} - \alpha_{gw}\theta\right) \tag{14}$$

Consequently the macroscopic stress, Eq. (10), can be written as

$$\boldsymbol{\sigma} = \frac{\partial \Psi}{\partial \boldsymbol{\varepsilon}} = (1-D)[2G\mathbf{e} + K(tr\boldsymbol{\varepsilon} - \alpha\theta)\mathbf{1}] - bp\mathbf{1} \tag{15}$$

The constitutive model is completed by the evolution equations for the variation of the wet gel volume content ζ_{gw} (defined in (1)) and the damage D. The rate of the gel content is assumed to be proportional to the rate of the reaction extent ξ, a phenomenological internal variable ($0 \leqslant \xi \leqslant 1$) used to describe both the gel formation and the gel swelling, considered as simultaneous, in accordance with the experimental results (see e.g. Haha et al. (2007)):

$$\dot{\zeta}_{gw} = c\dot{\xi} \tag{16}$$

The constant c in (16) is proportional to the free asymptotic volumetric expansion in the isothermal fully saturated case ϵ^{∞}_{ASR}. It's expression can be obtained from (10) by imposing the free-stress expansion condition ($\boldsymbol{\sigma} = \mathbf{0}$) and reads

$$c = \frac{K + Mb^2}{Mb}\epsilon^{\infty}_{ASR} \tag{17}$$

Considering a first order reaction kinetics, the following form for the reaction rate is proposed

$$\dot{\xi} = \frac{\langle f_{S_w} - \xi \rangle^{+}}{\tilde{t}}, \quad f_{S_w} = \frac{1 + b_1 \exp(-b_2)}{1 + b_1 \exp(-b_2 S_w)} \tag{18}$$

with b_1 and b_2 material parameters to be calibrated on the base of experimental data (see Section 2.4). In the fully saturated case, $S_w = 1$, the kinetic law given in Eq. (18) coincides with the one proposed by Larive (1998). Note that due to the presence of $f_{S_w} \leqslant 1$ in the evolution law, the limit value $\xi = 1$, corresponding to the complete development of the reaction, can be obtained in the fully saturated case only. In (18) $\tilde{t}$ is the intrinsic time of the reaction, which depends on the local histories of temperature $T(t)$, degree of saturation $S_w(t)$ and reaction extent $\xi(t)$. It is expressed in terms of both the latency time τ_{lat} and the characteristic time τ_{ch} registered for the swelling of reactive specimens and defined in Larive (1998). In the present work the following law is proposed

$$\frac{1}{\tilde{t}} = \frac{\xi/f_{S_w} + \exp\left(-\tau_{lat}/\tau_{ch}\right)}{\tau_{ch}(1 + \exp\left(-\tau_{lat}/\tau_{ch}\right))} \tag{19}$$

with

$$\tau_i(T, S_w) = \left\{ \tau_i(\overline{T}, 1) + \frac{\tau_i(\overline{T}, 0) - \tau_i(\overline{T}, 1)}{1 + c_{1i}\exp\left[-\frac{c_{2i}(1-2S_w)}{S_w(1-S_w)}\right]} \right\} \exp\left[U_i\left(\frac{1}{T} - \frac{1}{\overline{T}}\right)\right] \tag{20}$$

with $i = ch, lat$. In the expressions (20) the dependence on the temperature, described by the Arrhenius law as in Ulm et al. (2000), is combined with the dependence on the degree of saturation, based on experimental results at the reference temperature $\overline{T} = 38°C$; U_{lat} and U_{ch} are the activation energies; the parameters c_{1i}, c_{2i} are calibrated with experimental data. Fig. 4 shows the latency and the characteristic times as functions of both temperature and degree of saturation.

Even though the Eqs. (20) define the values of the latency and characteristic times for any degree of saturation, it should be remarked that, for degree of saturation lower than 0.6 no experimental values are available since the corresponding asymptotic expansion is almost zero. Therefore the values of the latency and characteristic times for low moisture contents are non influential.

The evolution of the damage variables D_t and D_c is governed by loading–unloading conditions defined in terms of the macroscopic stress $\boldsymbol{\sigma}$ and the wet gel pressure p through the "inelastic effective stress" $\boldsymbol{\sigma}''$ defined as

$$\boldsymbol{\sigma}'' = \boldsymbol{\sigma} + \beta p\mathbf{1} \tag{21}$$

The non-dimensional coefficient $\beta \leqslant b$ governs the damage level achievable in a reactive concrete specimen in a free expansion test. The loading–unloading conditions read

$$f_i \leqslant 0 \ \dot{D}_i \geqslant 0 \quad f_i\dot{D}_i = 0, \ i = t, c \tag{22}$$

where f_t and f_c are the damage activation functions in tension and compression, defined as

$$f_i = \frac{1}{2}\mathbf{s} : \mathbf{s} + a_{i0}(tr\boldsymbol{\sigma}'')^2 + a_{i1}tr\boldsymbol{\sigma}''h_i - a_{i2}h_i^2, \quad i = t, c \tag{23}$$

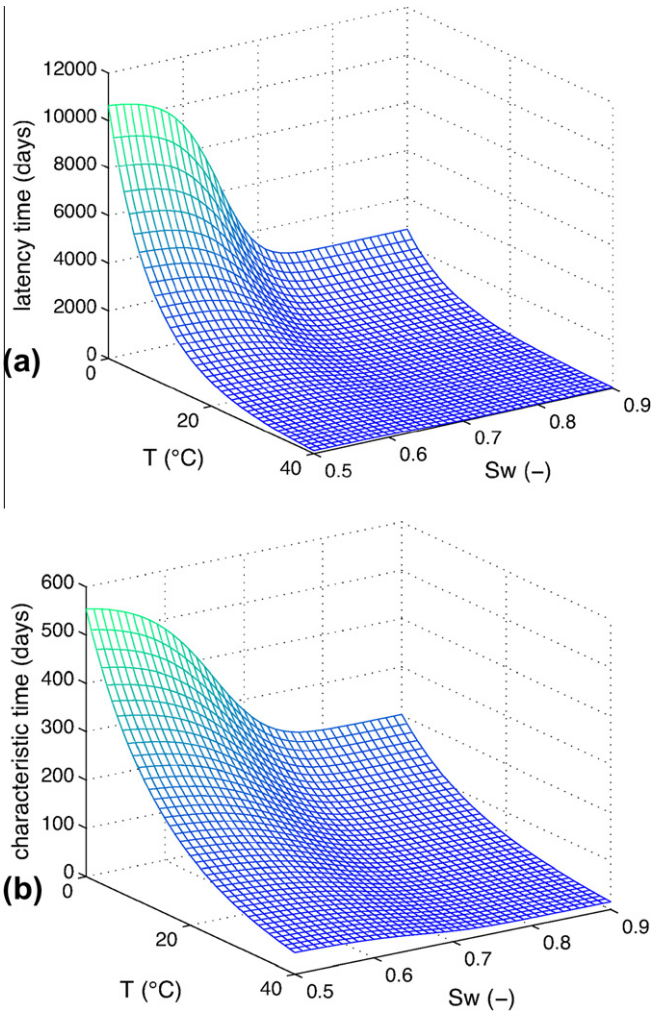

Fig. 4. Influence of temperature and degree of saturation (a): on the latency time (b): on the characteristic time.

where $\mathbf{s}$ is the deviatoric stress, a_{i0}, a_{i1}, a_{i2} $(i = t, c)$ are material parameters governing the shape and dimensions of the elastic domain (see Comi and Perego (2001) for details) and h_t and h_c are the hardening–softening functions

$$h_i(D_i) = \begin{cases} 1 - \left[1 - \left(\frac{\sigma_{ei}}{\sigma_{0i}}\right)\right]\left(1 - \frac{D_i}{D_{0i}}\right)^2 & \text{for} \quad D_i < D_{0i} \\ \left[1 - \left(\frac{D_i - D_{0i}}{1 - D_{0i}}\right)^{\gamma_i}\right]^{0.75} & \text{for} \quad D_i \geqslant D_{0i} \end{cases} \qquad i = t, c \tag{24}$$

where σ_{ei}/σ_{0i} is the ratio between the stress at the elastic limit and at peak in a uniaxial tension $(i = t)$ or compression $(i = c)$ test, D_{0i} defines the damage level corresponding to the peak stress in a uniaxial test, γ_i governs the negative slope of the softening part of the functions $h_i(D_i)$. In the finite-element implementation, the exponent γ_i is used to scale the fracture energy density of the material in such a way that each finite element can dissipate the correct amount of energy, independently of its size.

2.4. Model calibration

The proposed model requires the identification of three distinct sets of material parameters, namely: (i) elastic parameters for concrete skeleton and gel (K, G, M, b) (ii) parameters defining the expansion due to ASR (U_i, $\tau_i(\overline{T}, 1)$, $\tau_i(\overline{T}, 0)$, c_{i1}, c_{i2}, with $i = lat$, ch, ϵ^{∞}_{ASR}, b_1, b_2) (iii) parameters governing the damage response (β,a_{i0}, a_{i1}, a_{i2}, σ_{ei}/σ_{0i}, D_{0i}, $i = t, c$). The procedure for the choice of these parameters is briefly illustrated in the following.

(i) The elastic parameters for concrete can be computed from the experimental values of Young's modulus and Poisson ratio; Biot's parameters M and b can be obtained from the initial porosity ϕ of concrete through the relations proposed in Heukamp et al. (2001). The values of this set of parameters are reported in Table 1.

(ii) The activation energies U_{lat} and U_{ch} should be estimated on the basis of experiments on reactive specimens. In the present work we adopt the values identified by Larive (1998) by experiments at different temperatures. The calibration of the other parameters in Eq. (20), $\tau_i(\overline{T}, 1)$, $\tau_i(\overline{T}, 0)$, c_{1i}, c_{2i}, requires the knowledge of the free expansion curves at different moisture conditions. In particular $\tau_{lat}(\overline{T}, 1)$and $\tau_{ch}(\overline{T}, 1)$represent the latency time and the characteristic time of ASR in fully saturated conditions, $\tau_{lat}(\overline{T}, 0)$and $\tau_{ch}(\overline{T}, 0)$ represent the limit values for low degree of saturation, c_{1i} and c_{2i} tune the evolution between these limit values. Fig. 5 shows the experimental values taken from Larive (1998) and the curves obtained with the proposed model after parameter identification.
Parameters ϵ^{∞}_{ASR}, b_1 and b_2 (see Eqs. (17) and (18)) define the maximum axial expansion achievable in different moisture conditions

$$\epsilon_{\max}(S_w) = \frac{1 + b_1 \exp(-b_2)}{1 + b_1 \exp(-b_2 S_w)} \frac{\epsilon^{\infty}_{ASR}}{3} \tag{25}$$

These parameters have been calibrated by considering the maximum expansion measured by Larive (1998) and Multon (2003) in isothermal tests on reactive specimens characterized by different degree of saturation. The resulting model curve together with the experimental points is reported in Fig. 6. The values of the parameters thus identified are reported in Table 2.
Since the experimental results are often expressed in terms of change in mass, here they are converted into values of degree of saturation through the water content w, i.e. the ratio between the mass of water and the mass of solid. The degree of saturation S_w can be expressed in terms of w as $S_w = \gamma_w w/(\gamma_s e)$, where e is the void index, γ_w and γ_s are the specific weights of water and solid respectively. When the experimental results are expressed in terms of relative humidity, they can be converted in degree of saturation according to the procedure discussed in Section 2.2. In the simulation of the tests reported in Larive (1998), Multon (2003) and Multon and Toutlemonde (2010), whenever not specified, the initial degree of saturation is assumed equal to 0.6.

(iii) The parameters a_{i0}, a_{i1}, a_{i2}, σ_{ei}/σ_{0i}, D_{0i}, $i = t, c$ can be identified on the basis of standard uniaxial and biaxial mechanical tests on concrete. Feasible intervals for the model parameters can be found in Comi and Perego (2001) with reference to non reactive concrete. In the presence of ASR the addi-

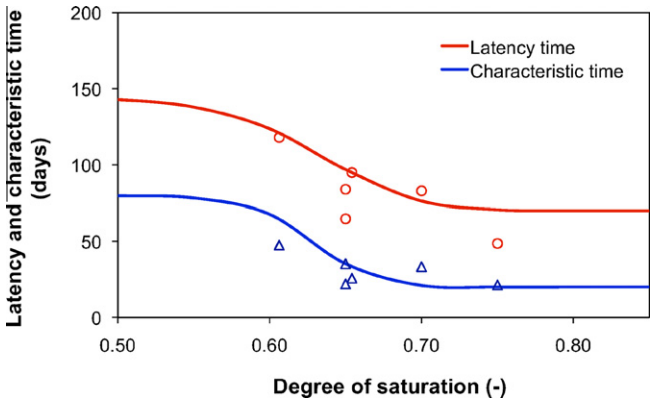

Fig. 5. Variation of the latency time and of characteristic time with the degree of saturation: experimental points from Larive (1998) and proposed model.

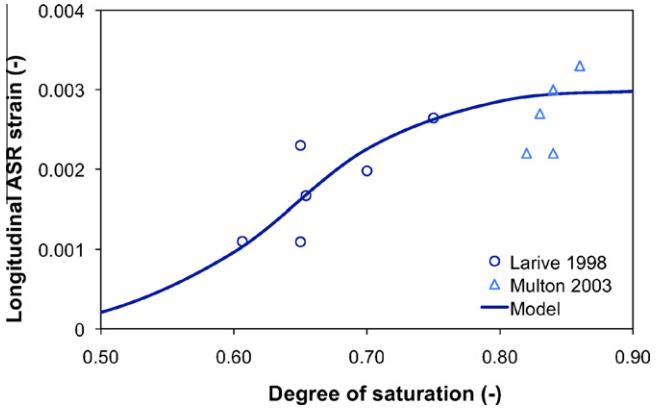

Fig. 6. Variation of the maximum free axial ASR expansion achievable in different moisture conditions: experimental points from Larive (1998) and Multon (2003) and proposed model.

Table 2
Calibrated parameters for the ASR model.

Parameter	Value	Unit	Parameter	Value	Unit
$\tau_{lat}(\overline{T}, 1)$	70	days	c_{1lat}	0.03	–
$\tau_{lat}(\overline{T}, 0)$	145	days	c_{2lat}	3.1	–
$\tau_{ch}(\overline{T}, 1)$	20	days	c_{1ch}	0.004	–
$\tau_{ch}(\overline{T}, 0)$	80	days	c_{2ch}	5.0	–
b_1	140000	–	U_{lat}	9400	K
b_2	18.5	–	U_{ch}	5400	K
ϵ^{∞}_{ASR}	0.009	–			

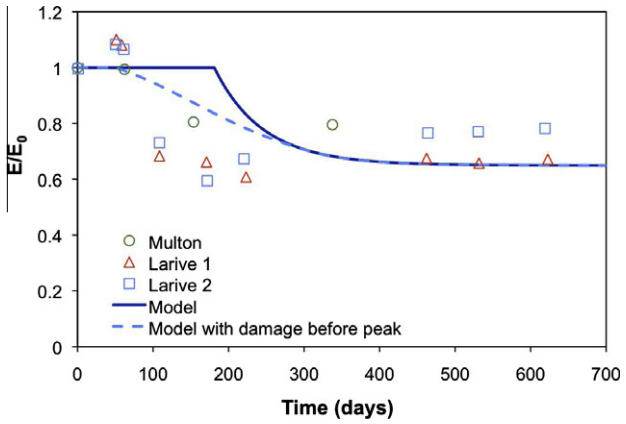

Fig. 7. Young's modulus reduction for reactive specimens subjected to free expansion tests: experimental points from Larive (1998) and Multon (2003) and model prediction.

tional parameter β can be calibrated starting from the experimental data on the Young's modulus degradation of reactive specimens in free expansion tests.

Fig. 7 shows the experimental values of the Young modulus, normalized with its initial value reported by Multon (2003) and Larive (1998) and the time evolution obtained with the proposed model after the identification of β. The continuous line is obtained with the values $D_{0t} = 0$ and $\sigma_{et}/\sigma_{0t} = 1$, i.e. assuming a linear elastic behavior in tension until the peak strength; the dashed line shows the behavior described by the model assuming $D_{0t} = 0.3$ and $\sigma_{et}/\sigma_{0t} = 0.6$. While the first assumption is the one commonly used in the absence of specific experimental data, the inclusion of a nonlinear behavior before the peak allows to obtain a more gradual reduction of the Young's modulus.

In the present work we have considered the experimental campaign of Multon (2003) and Multon and Toutlemonde (2006) on reactive concrete. Since only uni-axial mechanical tests have been performed and no experimental data are available concerning the biaxial behavior of that concrete, we have identified the parameters $a_{i0}, a_{i1}, a_{i2}, i = t,c$ on the basis of the uni-axial tension and compression strengths and of the deformation evolution measured in loaded and/or confined specimens. In fact while the free expansion predicted by the model only depends on the parameters governing the evolution of the ASR, the expansion curve in the presence of the compressive load and/or lateral confinement also depends on the damage activation conditions, and hence, on the parameters defining the activation functions f_t and f_c. In particular for the identification we have considered the mean deformation measured on cylindrical specimens loaded with an axial compression stress of 20 MPa (labeled as 0 mm_20MPa) and the mean deformation measured on specimens constrained by steel rings of 5 mm (labeled as 5 mm_0MPa). The symbols in Fig. 8 represent the experimental mean strain due to the chemical reaction only, since creep, shrinkage and instantaneous elastic strains have been subtracted; consistently the continuous curves representing the model response have been obtained by subtracting the elastic contribution from the total strains. In Fig. 8 also the free expansion curve (labeled 0 mm_0MPa) is shown for reference. Fig. 9 shows the activation functions in tension and compression in the effective stress plane $\sigma''_1 - \sigma''_2$ corresponding to the above calibrated parameters, reported in Table 3.

2.5. Model validation

To validate the form of the kinetic of the ASR proposed in this work, and in particular the proposed dependence on the degree

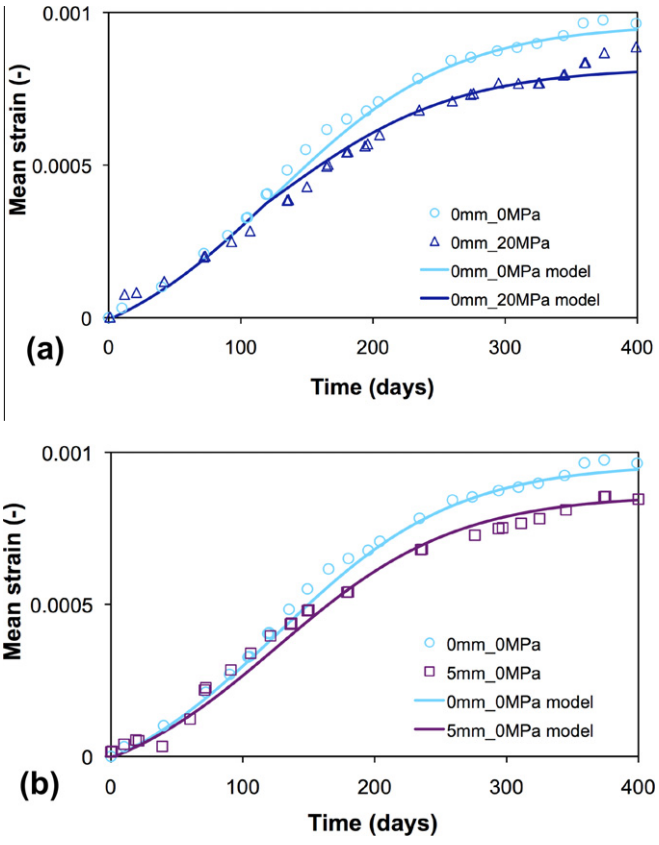

Fig. 8. Comparison between a free expansion test and (a) a loaded test (20 MPa), (b) a confined test (5 mm): experimental point from Multon and Toutlemonde (2006) and model prediction.

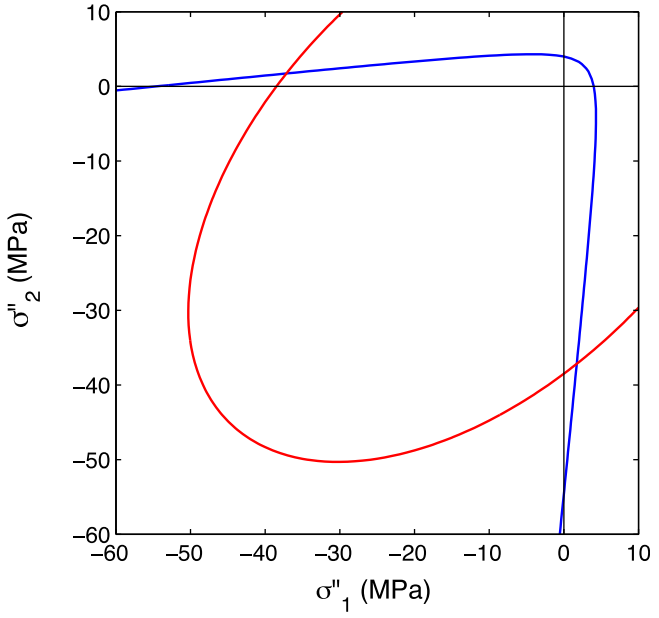

Fig. 9. Tension and compression damage activation functions for the calibrated parameters.

of saturation, we have simulated the isothermal tests by Larive (1998) on cylindrical specimens subjected to different moisture conditions. Fig. 10 shows the free expansion curves computed with the calibrated parameters, for $T = 38°C$ and for different degrees of saturation, corresponding to change in mass of 0.05%, 0.43% and 0.63%, and the corresponding experimental values. Then the model

Table 3
Calibrated parameters for the damage model.

Parameter	Value	Unit	Parameter	Value	Unit
a_{t0}	0.25	–	a_{c0}	0.0025	–
a_{t1}	4.31	MPa	a_{c1}	3.80	MPa
a_{t2}	18.62	MPa^2	a_{c2}	349.29	MPa^2
β	0.0287	–			

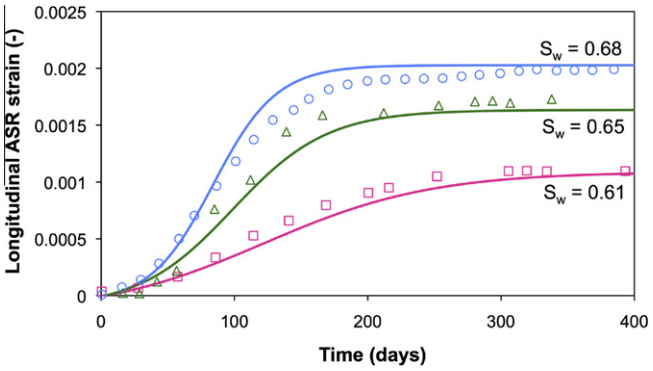

Fig. 10. Free axial ASR expansion at T = 38 °C for different degree of saturation: experimental points from Larive (1998) and proposed model.

has been employed to simulate the experiments by Multon and Toutlemonde (2010) on cylindrical specimens kept in water after the 28 curing days or kept in air at 100% relative humidity (RH) for 676 days and then immersed in water. The late water supply causes supplementary expansion and the strain tends to reach the value corresponding to specimens immersed in water after 28 curing days. The experimental points and the model prediction are compared in Fig. 11; a good agreement is observed.

2.6. The heat and humidity characteristic lengths

The ASR development in a real structure depends on the temperature and humidity fields and on their variation during its service life.

In order to study the influence of heat transport on the advancement of the reaction in concrete structures affected by ASR, Ulm et al. (2000) consider the solution of the heat transport equation in a semi-infinite half-space ($x \geqslant 0$) with initial temperature T_0, delimited by a plane Γ maintained at a constant temperature $T_\Gamma > T_0$, under uniform moisture conditions. The solution of the above problem depends on the thermal diffusion length $\sqrt{D_T t}$, D_T being heat diffusivity of concrete (m^2/days), so that $T \simeq T_\Gamma$ near the heated surface for $x \ll \sqrt{D_T t}$ and $T \simeq T_0$ for $x > \sqrt{D_T t}$. This analysis allows to define the zone where, at a given time, ASR takes place. To this purpose, to simplify the problem, one can assume a step evolution of the reaction extent instead of Eq. (18), so that $\xi = 0$ for $t < \tau_{lat}(T)$ and $\xi = 1$ for $t \geqslant \tau_{lat}(T)$. Since the latency time of the reaction $\tau_{lat}(T)$ diminishes with the temperature T, $\xi(t) = 0$ everywhere for $t < \tau_{lat}(T_\Gamma)$ and $\xi(t) = 1$ everywhere for $t > \tau_{lat}(T_0)$. For a time $\tau_{lat}(T_\Gamma) \ll t < \tau_{lat}(T_0)$ the reaction activates (that is $\xi(t) = 1$ considering a step function) only in the zone $x < l_T$ identified by the characteristic thermal length $l_T = \sqrt{D_T \tau_{lat}(T_\Gamma)}$. In the presence of both thermal and humidity gradients, taking advantage of the analogy between the moisture diffusion law in (6) and the Fourier heat transport law, it is possible to define two characteristic lengths, l_T and l_w, defining the zone in which combined effects of diffusion (of heat or moisture) and ASR occur.

$$l_T = \sqrt{D_T \tau_{lat}(T_\Gamma, S_{w,\Gamma})}, \quad l_w = \sqrt{D_w(S_{w,\Gamma}) \tau_{lat}(T_\Gamma, S_{w,\Gamma})} \tag{26}$$

where D_w is the permeability defined by (7), T_Γ and $S_{w,\Gamma}$ are the temperature and the degree of saturation applied to the plane Γ.

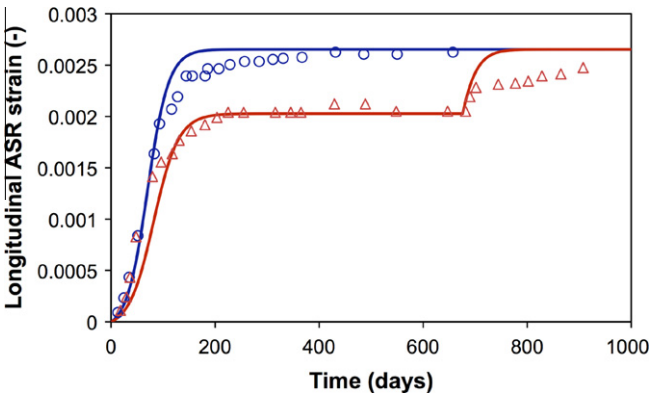

Fig. 11. Free expansion tests at T = 38 °C with late water supply: experimental data from Multon and Toutlemonde (2010) and model prediction.

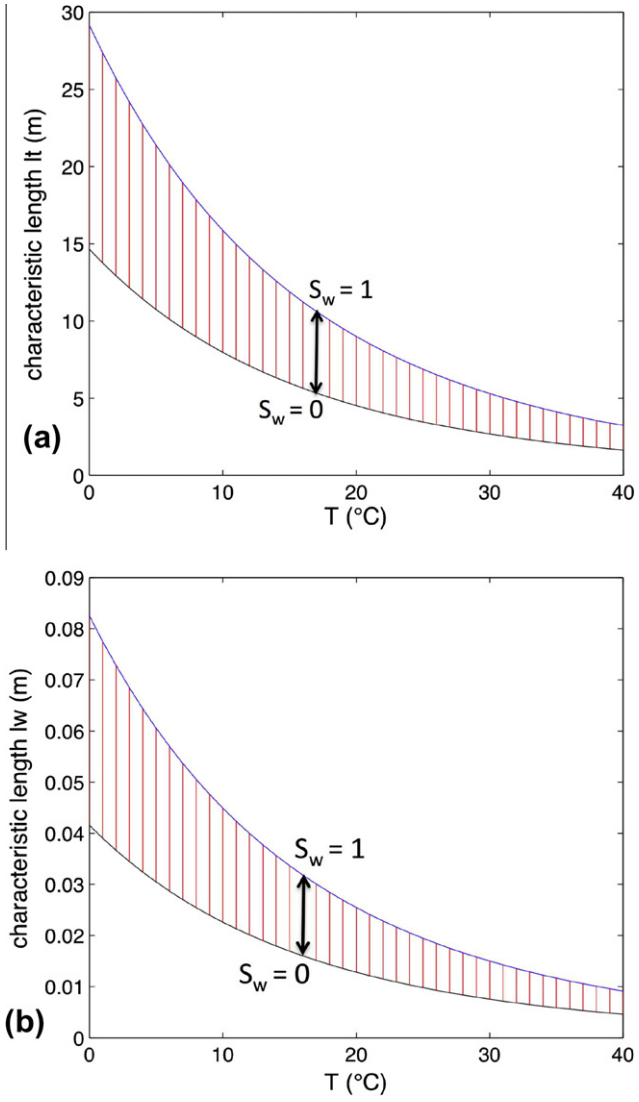

Fig. 12. Simultaneous influence of temperature and degree of saturation on the temperature and moisture characteristic lengths l_T and l_w.

Fig. 12 shows the characteristic lengths as functions of temperature and degree of saturation (each vertical segment, at fixed T, corresponds to S_w varying from 0 to 1). As shown in Fig. 12, with the diffusivity parameters of concrete, the heat characteristic length l_T is two orders of magnitude higher than the moisture characteristic length l_w. In massive structures (as gravity dams), where the dimensions are of the same order of magnitude of the temperature characteristic length and much bigger than the moisture characteristic length, non-uniform temperature boundary conditions cause temperature gradients in the whole structure, bringing to differential ASR expansion, while varying moisture boundary conditions can affect only the superficial layer of the structure, so that the overall behavior of the structure is governed by the initial humidity condition in the body of the structure. This aspect will be further discussed in Section 3.2. On the contrary humidity gradients can be important in slender structures, where the structural dimensions are comparable with the moisture characteristic length l_w.

3. Structural analysis of damage induced by the alkali–silica reaction

3.1. Reactive plain and reinforced concrete beams submitted to moisture gradients

The proposed model has been validated by simulating the experimental tests performed by Multon and Toutlemonde (2010) on reactive plain and reinforced concrete beams. In that experimental campaign, aimed to investigate the effects of varying humidity conditions on the ASR development, after curing under aluminium sealing, the lower face of the beams was immersed in water, while the upper face was dried with air at 30% RH for 14 months and then submitted to a delayed water supply for 9 months (see Fig. 13).

The constitutive model developed in the present work has been implemented in the commercial finite-element code Abaqus through Fortran user's subroutines. The mesh dependence due to the strain localization typical of damageable materials has been prevented adopting a so called "fracture energy regularization" as in Comi et al. (2009). For the numerical simulation of the beams we have employed a three-dimensional mesh with twenty nodes brick elements. Exploiting symmetries only one quarter of the beams has been modeled.

The elastic parameters and the permeability parameters used in this simulation are reported in Table 1, the parameters for the ASR model are those calibrated in Section 2.4 and reported in Table 2.

First of all a moisture diffusion analysis has been performed to compute the history of the degree of saturation and the corresponding reaction extent history at each point. The formal analogy between the non-linear transport law for moisture in its liquid form (6) and the Fourier equation commonly used for the heat transport permits to use the standard Abaqus heat transfer analysis both for the heat and moisture diffusion analyses, by introducing a non-linear conductivity coefficient in the second case.

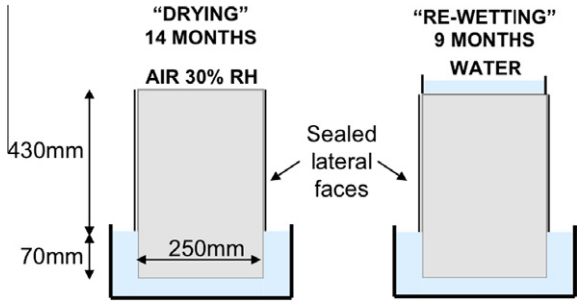

Fig. 13. Moisture conditions of the beams tested by Multon and Toutlemonde (2010).

Fig. 14 shows the computed patterns of degree of saturation and reaction extent after 14 and 23 months respectively. The reaction starts in the lower part of the beam, where humidity is higher, and then, after water supply, develops in the upper part. Then a chemo-mechanical analysis has been performed with the proposed model. Fig. 15 shows the contour plot of damage in the plain beam (a) and in the reinforced beam (b). The presence of reinforcement reduces the achieved damage level.

The comparison between experimental results and numerical analysis is shown in Fig. 16 for the plain beam in terms of vertical (a) and transversal (b) strain evolution at different depths of the beam, as indicated on the section of the beam in the same figure. A good qualitative agreement is observed except for the upper point considered. Indeed at 0.08 m from the top of the beam the model does not predict any swelling in the first drying phase, while the experimental data show a limited expansion which seems to indicate that ASR is not completely stopped. This discrepancy can be attributed to the lack of information about the exact initial humidity field inside the beam and hence to an uncorrect estimate of the initial field of the degree of saturation.

Figs. 17 and 18 respectively compare the experimental and the computed values of the longitudinal strain, with reference to the depth of 23 cm from the top of the beam, and the maximum deflection both for the plain and the reinforced beam. The presence of reinforcement constrains the concrete swelling and significantly reduces the overall structural effect of ASR. This effect is correctly reproduced by the proposed model.

The quantitative discrepancy between experimental data and model results, in particular the delay of the expansion in the re-wetting phase, could be partially caused by the difference between the moisture pattern obtained with the theoretical diffusion law in (25) and the real adsorption–desorption behavior of the beam. This aspect is evidenced in Fig. 19 which compares the experimental results with the model predictions in terms of mass variation along the beam depth. Fig. 19a shows the advancement of the wet and drying front respectively in the lower and upper parts of the beams at the end of the first phase of the humidity history, Fig. 19b shows the advancement of the wet front both in the lower and the upper part due to the delayed wetting of the beams (the last 9 months): even though there is an overall qualitative agreement, point wise there are significant quantitative differences. A careful calibration of the permeability parameters could improve the results but it would require experimental measures of specimens drainage and imbibition for the concrete under examination. Since these experimental data were not available, we have used the permeability parameters reported in the literature for concrete, as explained in Section 2.2.

3.2. Concrete gravity dam

The proposed model has been also employed to simulate the behavior of a gravity dam, subjected to service loading and affected by the ASR. Reference was made to the right gravity dam of the Beauharnois power plant (Québec, Canada). The construction of the plant begun in 1932 and the right gravity dam was completed in 1941. This dam displayed cracks due to ASR and the grouting of cracks started in 1947, only six years after the construction (Bérubé et al., 2000). Afterwards several retrofitting provisions were taken including the adoptions of post-tension cables and the repair of surface concrete, and some expansion slots were cut in the structure to release the eigenstress state. According to measurements which had been taken since early 1970's and reported in Kladek et al. (1995), despite these provisions the displacements rates

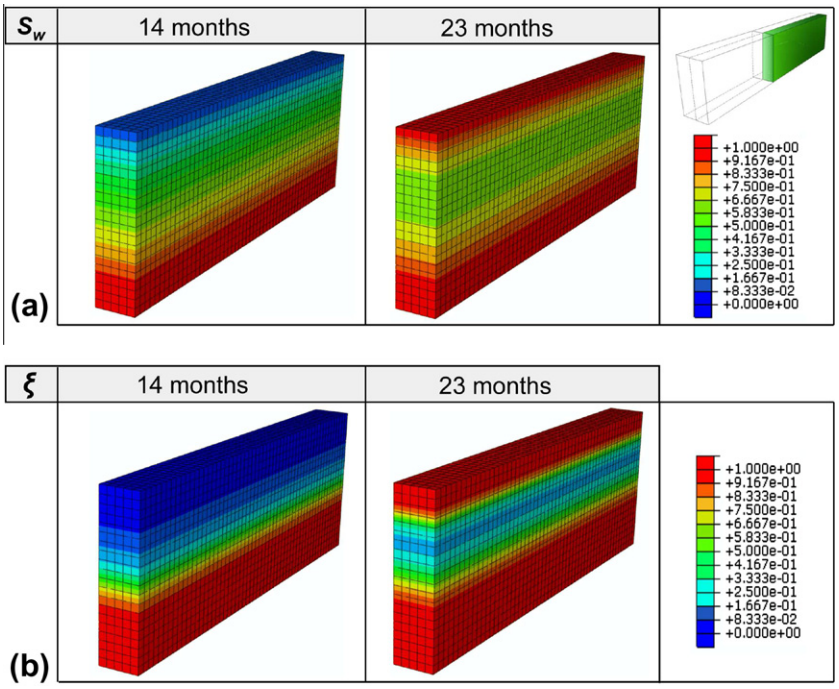

Fig. 14. Patterns of (a) degree of saturation and (b) reaction extent after 14 and 23 months.

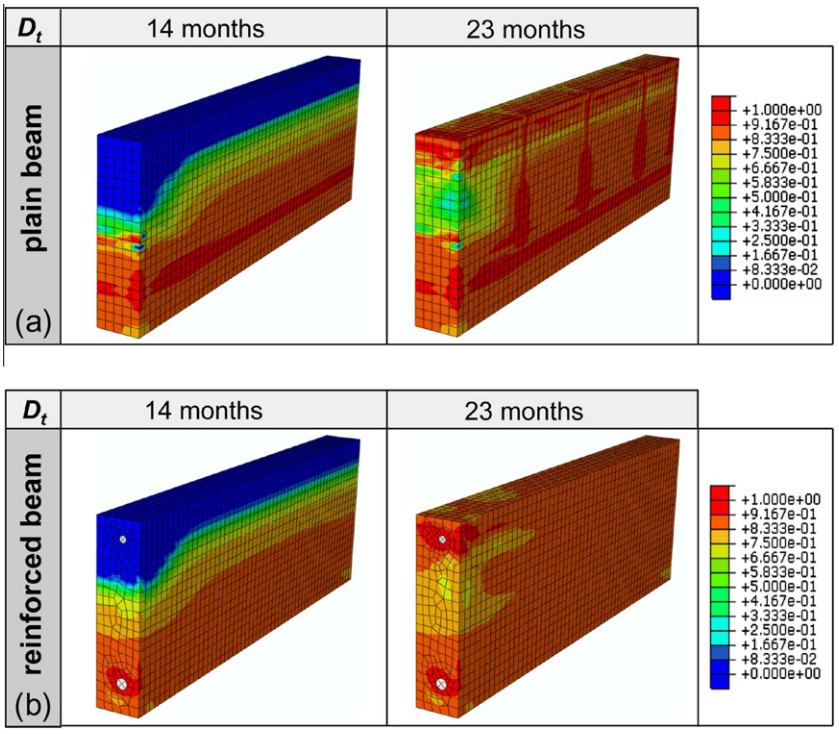

Fig. 15. Patterns of the damage level in the (a) plain and (b) reinforced beams after 14 and 23 months.

where constant over two decades and equal to 2.2 mm/year in the horizontal upstream direction for a particular section and equal to 0.6 mm/year for another section of the dam. Mechanical experimental tests conducted on drilled specimens between 1985 and 1988, about 45 years after the construction, when the dam was already seriously damaged, gave a compressive stress around 44 MPa, a Young's modulus of 18 GPa and a splitting strength ranging from 1.6 to 3.4 MPa, as reported in Raphael et al. (1989).

The geometry and the loads assumed in the numerical analysis are shown in Fig. 20 (see Huang and Pietruszczak (1999)). A period of 60 years after the construction is considered in the analysis.

The chemical and mechanical properties of concrete are assumed homogeneously distributed in the body of the dam. The initial mechanical properties of the concrete to be used in the analysis are estimated as follows. Since various experimental campaigns on reactive specimen show that the reduction of compressive strength

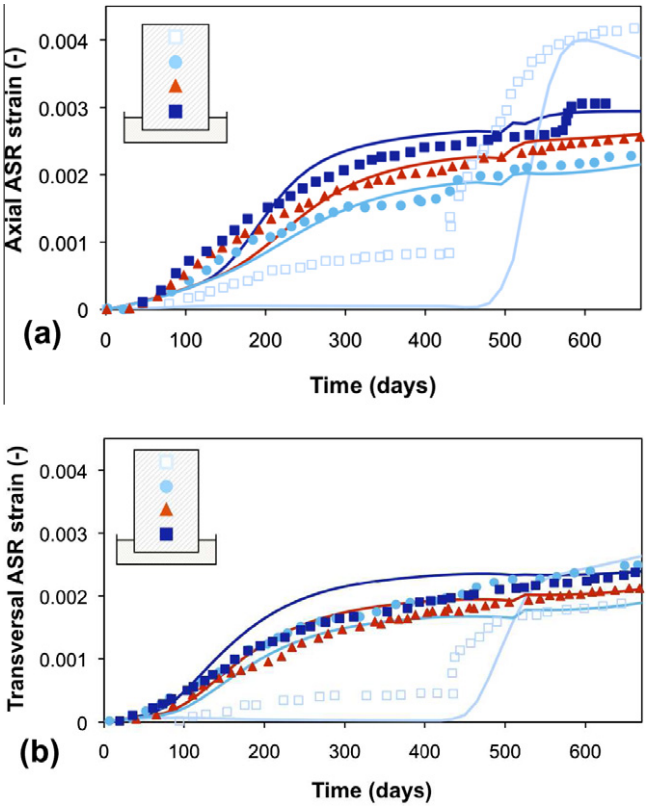

Fig. 16. Vertical (a) and transversal (b) strains of reactive beams measured at four depths (0.08, 0.17, 0.27, 0.37 m from the upper face): experimental points from Multon and Toutlemonde (2010) and model prediction.

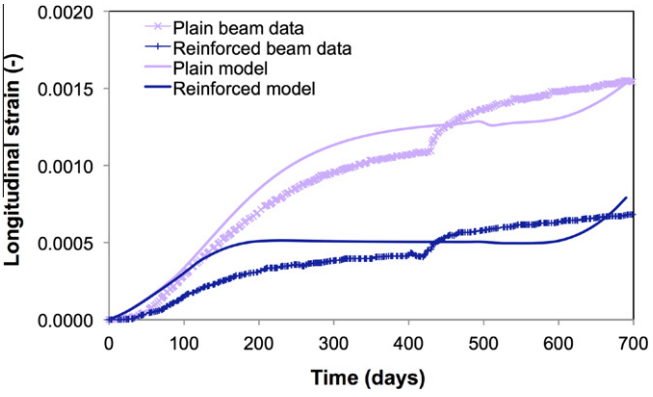

Fig. 17. Longitudinal strain for plain and reinforced beams: experimental evolution from Multon and Toutlemonde (2010) and model results.

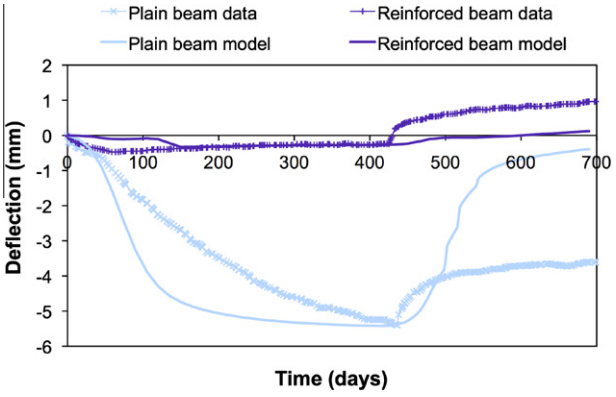

Fig. 18. Deflection for plain and reinforced beams: experimental evolution from Multon and Toutlemonde (2010) and model results.

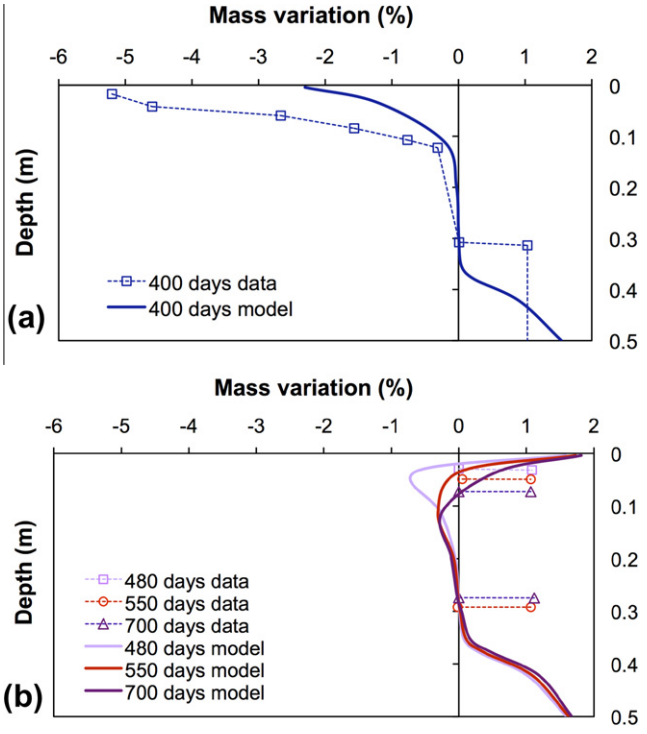

Fig. 19. Mass variation (a) immediately before (400 days) and (b) after (480, 550, 700 days) the re-wetting of the beam: experimental points from Multon and Toutlemonde (2010) and model prediction.

due to ASR is limited and often only counterbalance the increase due to continued hydration, we assumed the measured value reported in Raphael et al. (1989) as representative of the strength at 28 days so that the concrete can be classified according to the model code CEB as a C40 concrete grade (see CEB (1990)). The initial Young's modulus and the tensile strength are then given in this code, namely E = 36 GPa $\times$ 0.7 = 25 GPa (the coefficient 0.7 accounts for the aggregate type, sandstone for the Beauharnois dam) and σ_t=3.5 MPa. These initial values are reasonably correlated with the ones measured after 45 years from the construction on the concrete specimens deteriorate by ASR (a reduction of 28% for the Young's modulus and a reduction in the range 3–50% for the tensile strength). Fracture energy in tension and compression typical of a concrete characterized by large aggregate size have been assumed: G_{ft} = 0.3 Nmm^{-1} and G_{fc} = 30 Nmm^{-1} respectively. Since the value of the asymptotic expansion ϵ^{∞}_{ASR} is not available in the literature for the concrete used in the Beauharnois dam, various analyses have been made, comparing different values of the asymptotic axial ASR expansion, taken in a reasonable range for reactive concrete (0.0015 ÷ 0.002). Moreover longer values of both the latency and the characteristic times in saturated conditions ($\tau_{lat}(\overline{T},1)$ = 80 days and $\tau_{ch}(\overline{T},1)$ = 150 days) and a smaller value for the coefficient β (β = 0.018) have been used, in order to compare the results with the few available real data. The material parameters are collected in Table 4. A plane-strain mesh with triangular elements with one Gauss point has been employed.

Since the ASR is driven by the history of temperature and humidity, the mechanical analysis has been preceded by a heat transport analysis governed by the Fourier equation and a humidity diffusion analysis governed by the equation (6). Dirichlet

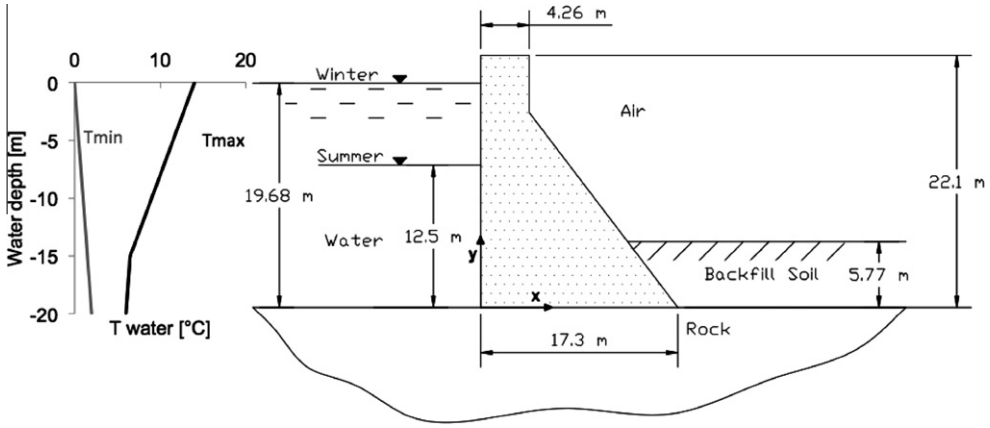

Fig. 20. Beauharnois gravity dam: geometry and loading conditions.

Table 4
Elastic parameters and parameters for the ASR model used for the simulation of the Beauharnois dam.

Parameter	Value	Unit	Parameter	Value	Unit
E	25000	MPa	$\tau_{lat}(\overline{T},1)$	80	days
v	–	–	$\tau_{lat}(\overline{T},0)$	200	days
σ_t	3.5	MPa	$\tau_{ch}(\overline{T},1)$	150	days
σ_c	44	MPa	$\tau_{ch}(\overline{T},0)$	300	days
G_{ft}	0.3	Nmm^{-1}	ϵ^{∞}_{ASR}	0.0045	–
G_{fc}	30	Nmm^{-1}			

conditions are imposed everywhere along the dam boundary. The minimum and maximum temperature of air, soil and water (the latter varying with the reservoir depth as shown in Fig. 20) reported in Huang and Pietruszczak (1999) are adopted and an harmonic variation with a period of one year is assumed, as shown in Fig. 21. The humidity history is assumed in phase with the seasonal oscillation of the reservoir water level and in opposition of phase with the environmental temperatures, which are lower in winter and higher during the summer (Fig. 21). The points of the upstream surface of the dam are subject to temperature and humidity changing between the air and the water temperature and humidity profiles, according to the reservoir water level oscillation.

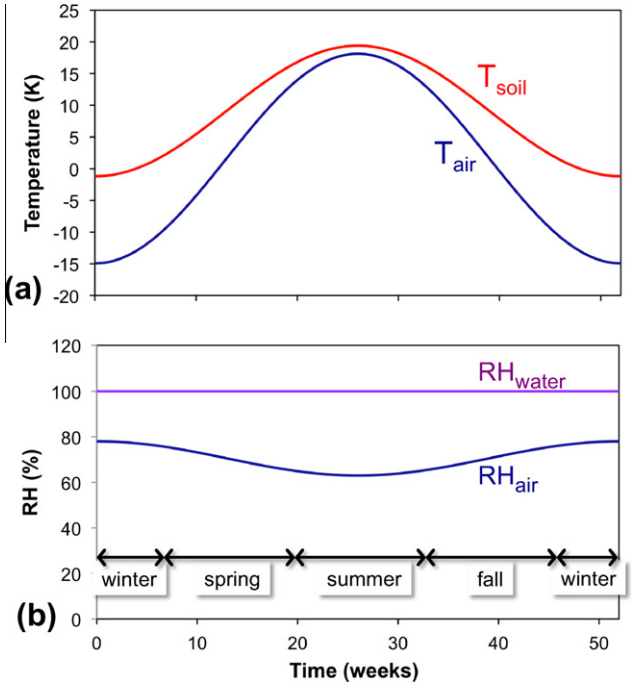

Fig. 21. Temperature and humidity variable boundary conditions.

In order to reduce the computing time of the transient analysis necessary to obtain the periodic stabilization of the temperature and the humidity oscillations, the stationary temperature T_0 and humidity S_{w0} fields have been computed preliminary, by imposing along the dam boundary the mean values of temperature and humidity histories. By assuming the stationary temperature and humidity fields as initial condition at $t = 0$, the transient heat-conduction and moisture-diffusion problems are solved with the periodic boundary conditions shown in Fig. 21. The thermal parameters are assumed constant while the permeability D_w is a function of the degree of saturation as in Eq. (7). The solution of the heat and moisture diffusion problem is the input for the chemo-mechanical problem.

Fig. 22 reports the histories of temperature, humidity and reaction extent at three different points of the dam and shows the prevalent effect of the humidity on the final reaction extent and the predominant effect of the temperature on the reaction kinetic in the first 1000 weeks. Fig. 23 displays the final patterns of degree of saturation and temperature in winter. Since the structural dimensions are comparable with the heat characteristic length but are much bigger then the humidity characteristic length (both defined in Eq. (26)), an important temperature gradient can be observed, while, on the contrary, the moisture diffusive process affects the external boundary of the structure only for a depth of about 40 cm and the degree of saturation is constant elsewhere, equal to the imposed initial value of 0.93.

Fig. 24 shows the reaction extent and the damage at three different time steps. At the beginning the damage appears only on the external skin of the structure, the only one affected by the external humidity conditions. The first macroscopic crack in the body of the dam and visible on the surface of the structure appears six years after the construction, in accordance with the data reported in Bérubé et al. (2000). Fig. 25 shows the horizontal crest displacements for different values of the asymptotic axial ASR expansion. The constant displacement rate predicted by the model after the first decade is between 0.5 and 0.8 mm/years. These values well compare with the displacement rate measured on the dam in the twenty years period of monitoring, highlighted in the zoomed view in Fig. 25.

Several comments on the dam structural analysis are worthwhile. (i) In the above analysis we have not simulated the retrofitting provisions that were taken during the life of the dam,

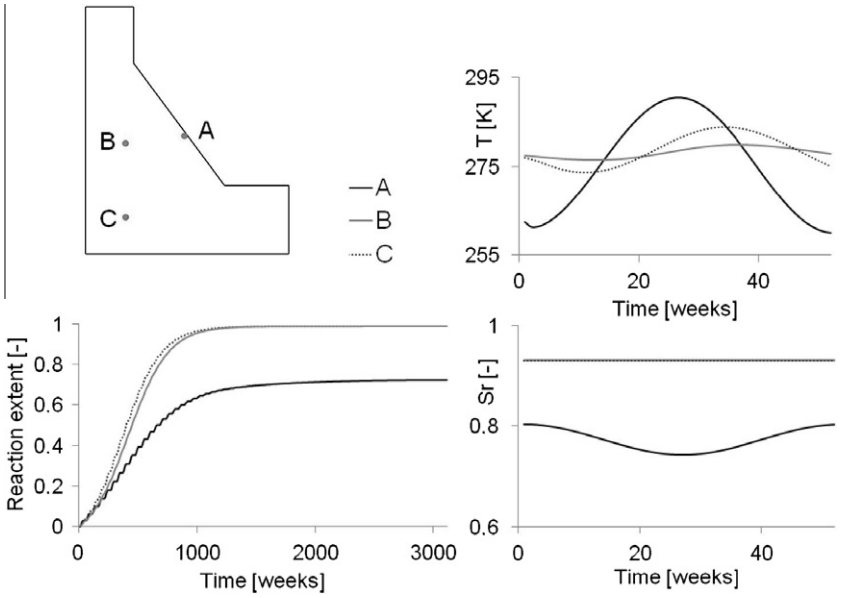

Fig. 22. Simultaneous influence of temperature and degree of saturation on the reaction extent: histories of temperature, degree of saturation and reaction extent at three different points.

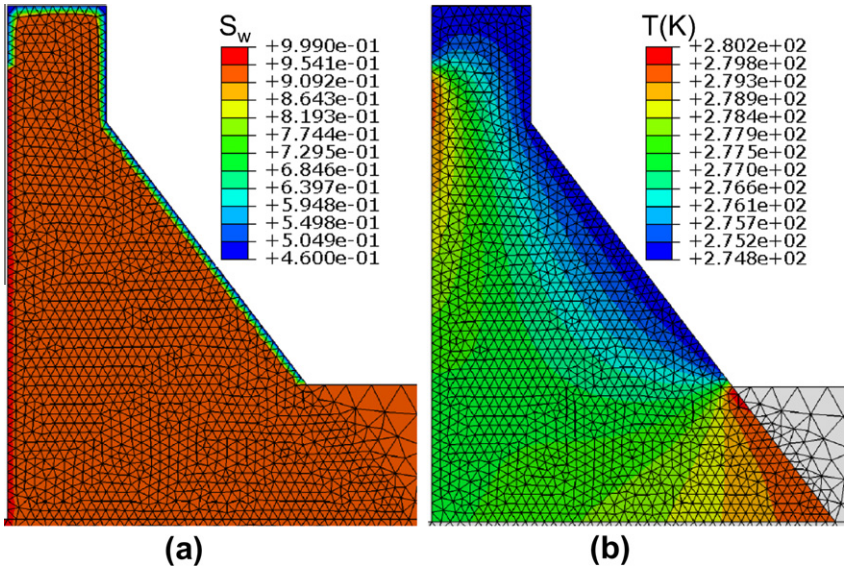

Fig. 23. Patterns of (a) degree of saturation and (b) temperature in K at the end of the analysis.

therefore the performed analysis is not representative of the real behavior of the dam, but is intended to show the applicability of the proposed model and analysis strategy to structural problems. (ii) The material parameters defining the mechanical behavior and the reaction development have been fixed using the few available experimental information. To correctly predict the behavior of a very complex structure such as a dam along various decades one should probably couple the proposed analysis with structural monitoring data in order to properly identify the material parameters on the basis of the past structural response. (iii) Since in a gravity dam the degree of saturation is close to one in the whole body dam, as expected in the case of gravity dams, the influence of the moisture is very limited and the overall behavior could be well approximated considering the temperature influence only. However the gradient of moisture near the downstream surface allow to reproduce the crack pattern which is experimental observed. This cracking, appearing after some years from the construction, is the first manifestation of ASR development. Moreover in other structures such as buttress dams or bridges, where the structural dimensions are comparable with the moisture diffusion length, the effect of moisture gradients can be important, as pointed out by Ulm et al. (2000) and shown in the present work with the example of beams subject to moisture gradient in Section 3.1. (iv) The hypothesis of isotropic damage at the material point level allows to simplify the model; the anysotropy of the cracked pattern is recovered at the structural level by oriented band of severely damaged material (as in Fig. 24). The assumption of an anisotropic model, as proposed e.g. in Comi and Perego (2011), allowing for a better description of the material behavior pointwise, would introduce additional parameters difficult to be identified. (v) Since the ASR develops during several decades of service life, other long term effects such as creep should be properly described.

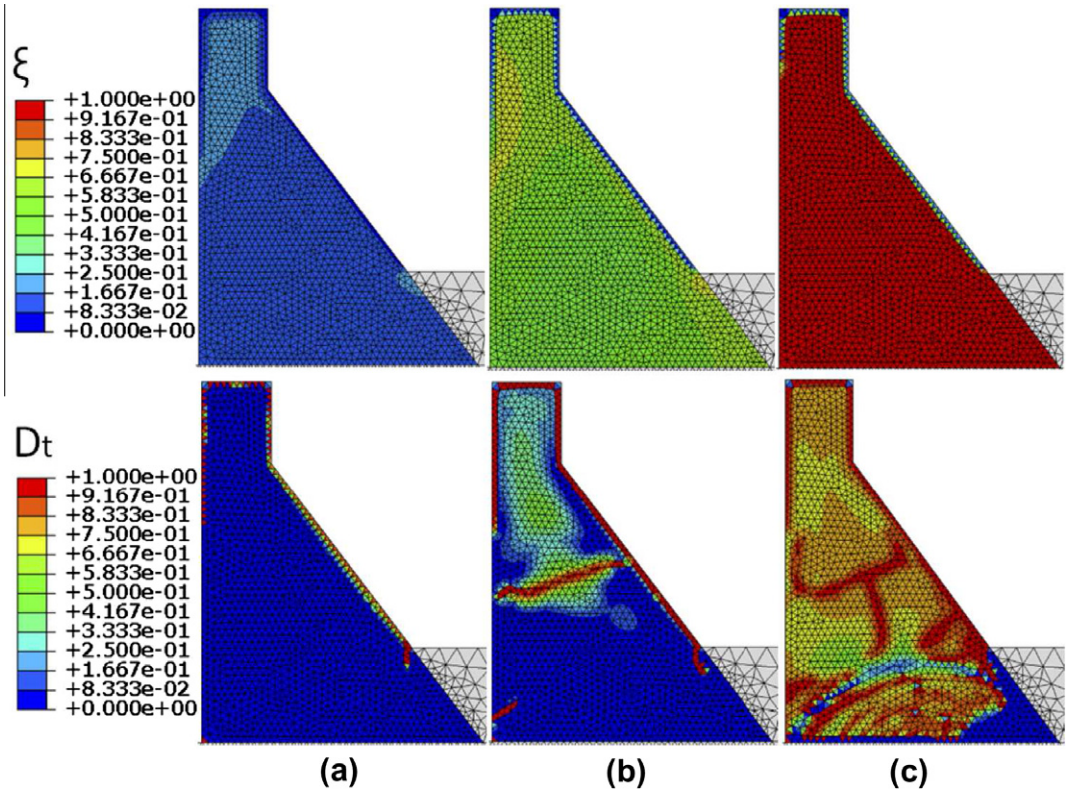

Fig. 24. Patterns of the reaction extent and damage after (a) 3, (b) 6 and (c) 60 years.

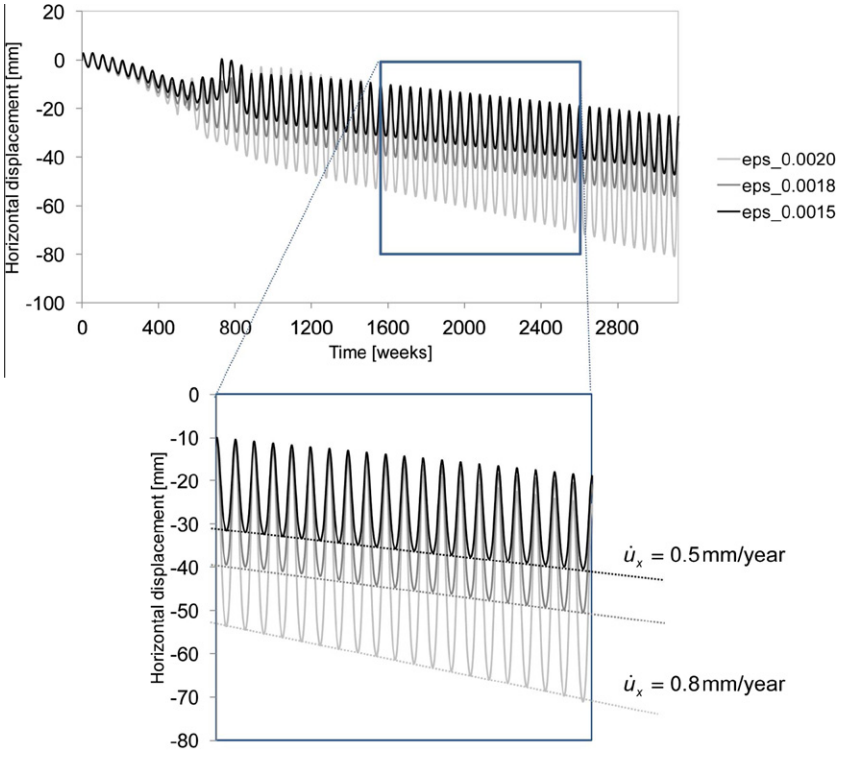

Fig. 25. Horizontal crest displacements for different values of the asymptotic axial ASR expansion.

4. Conclusions

A mathematical formulation has been developed for modeling the mechanical effects of the ASR in the presence of simultaneous temperature and moisture variations.

The constitutive relations have been formulated within the framework of the Biot's theory of multi-phase materials. The progressive expansion of the alkali–silica gel is described by a phenomenological internal variable. The swelling of the gel in the presence of moisture is resisted by concrete skeleton and causes the development of pressure which can damage the concrete surrounding the reactive sites. Both the effects of temperature and humidity on the kinetic of the chemical reaction and on the final value of the consequent expansion are included in the proposed model. A relatively simple model for the kinetics of ASR is proposed, in which temperature and humidity affect the latency and the characteristic time of the reaction.

Possible moisture and temperature gradients due to variable boundary conditions are taken into account through a heat transport analysis and a diffusion analysis of moisture in its liquid form. The different role of moisture and temperature in slender and massive structures affected by ASR has been discussed.

These diffusion analyses are firstly carried out, then the chemo-mechanical analysis is performed starting from the values of temperature and humidity preliminary calculated. The model has been validated by comparing the results numerically obtained by the proposed formulation with the experimental results reported in literature for reactive specimens and plain and reinforced beams. A good agreement is observed both in the case of homogeneous moisture conditions and in the presence of humidity gradients. In the latter case the model is capable to qualitatively catch the different behavior that beams subjected to moisture gradients show in different directions. A structural simulation of a gravity dam aimed at assessing the extent of structural damage caused by the reaction is also presented. In spite of the scarce informations on the real behavior of the dam, the model is able to qualitatively reproduce the structural consequences of ASR.

The enhancement of the model, in order to include other long term phenomena such as creep, is currently under development.

Acknowledgements

The authors acknowledge Luigi Flotta for his contribution to the numerical analyses.

References

Ahmed, T., Burley, E., Rigden, S., 2003. The effect of alkali reactivity on the mechanical properties of concrete. Construction and Building Materials 17, 123–144.

Baroghel-Bouny, V., Mainguy, M., Lassabatere, T., Coussy, O., 1999. Characterization and identification of equilibrium and transfer moisture properties for ordinary and high performance cementitious materials. Cement and Concrete Research 29, 1225–1238.

Bérubé, M.-A., Durant, B., Vézina, D., Fournier, B., 2000. Alkali–aggregate reactivity in Québec (Canada). Canadian Journal of Civil Engineering 27, 226–245.

CEB, 1990. CEB-FIP Model Code. Comite Euro-International du Beton.

Charlwood, R., 1994. A review of alkali aggregate in hydro-electric plants and dams. Hydropower Dams 5, 31–62.

Chatterji, S., Christensen, P., 1990. Studies of alkali–silica reaction. Part 7. Modeling of expansion. Cement and Concrete Research 20, 285–290.

Comi, C., Perego, U., 2001. Fracture energy based bi-dissipative damage model for concrete. International Journal of Solids and Structures 38, 6427–6454.

Comi, C., Perego, U., 2011. Anisotropic damage model for concrete affected by alkali–silica reaction. International Journal of Damage Mechanics 20, 598–617.

Comi, C., Pignatelli, R. 2010. On damage modeling of concrete affected by alkali–silica reaction in the presence of humidity gradient. in: XVIII GIMC Conference.

Comi, C., Pignatelli, R. 2011. A three-phase model for damage induced by ASR in concrete structures. in: IV International Conference on Computational Methods for Coupled Problems in Science and Engineering.

Comi, C., Fedele, R., Perego, U., 2009. A chemo–thermo-damage model for the analysis of concrete dams affected by alkali–silica reaction. Mechanics of Materials 41, 210–230.

Coussy, O., 2004. Poromechanics. John Wiley and Sons, New York.

Fairbairn, E.M.R., Ribeiro, F.L.B., Lopes, L.E., Toledo-Filho, R.D., Silvoso, M.M., 2006. Modelling the structural behaviour of a dam affected by alkali–silica reaction. Communications in Numerical Methods in Engineering 22, 1–12.

Farage, M.C.R., Alves, J.L.D., Fairbain, E.M.R., 2004. Macroscopic modelling of concrete subjected to alkali–aggregate reaction. Cement and Concrete Research 34, 495–505.

Grimal, E., Sellier, A., Le Pape, Y., Bourdarot, E., 2008. Creep, shrinkage, and anisotropic damage in alkali–aggregate reaction swelling mechanism – Part I: A constitutive model. ACI Material Journal 105 (3), 227–235.

Gudmundsson, G., Asgeirsson, H. 1983. Parameters affecting alkali expansion in icelandic concretes. in: Proceedings 6th International Congress on Alkali- Silica Reactions, Copenhagen, Denmark.

Haha, Ben, Gallucci, M., Guidoum, E., L., A., K.L., Scrivener, 2007. Relation of expansion due to alkali silica reaction to the degree of reaction measured by SEM image analysis. Cement and Concrete Research 37, 1206–1214.

Heukamp, F., Ulm, F., Germaine, J., 2001. Mechanical properties of calcium-leached cement pastes triaxial stress states and the influence of pore pressures. Cement and Concrete Research 31, 767–774.

Huang, M., Pietruszczak, S., 1999. Modeling of thermomechanical effects of alkali–silica reaction. Journal of Engineering Mechanics 125 (4), 476–485.

Kladek, I., Pietruszczak, S., Gocevski, V. 1995. Modelling of mechanical effects if alkali–silica reaction in Beauharnois powerhouse. in: Proceedings 5th International Symposium on Numerical Models in Geomechanics, Davos, Switzerland, 639–645.

Larive, C. 1998. Apports combinés de l'expérimentation et de la modélisation la comprehénsion de l'alcali-réaction et de ses effets méchaniques. Ph.D. thesis, LCPC.

Léger, P., Côte, P., Tinawi, R., 1996. Finite element analysis of concrete swelling due to alkali–aggregate reactions in dams. Computers and Structures 60 (4), 601–611.

Li, K., Coussy, O., Larive, C. 2004. Modelisation chimico-mecanique du comportement des beton affectes par la reaction d'alcali-silice. Laboratoires Central des Pontes et Chaussées.

Mainguy, M., Coussy, O., Baroghel-Bouny, V., 2001. Role of air pressure in drying of weakly permeable materials. Journal of Engineering Mechanics 127 (6), 582–592.

Multon, S. 2003. Evaluation expérimentale et théorique des effects mechaniques de l'alcali-réaction sur des structures modéles. Ph.D. thesis, LCPC.

Multon, S., Toutlemonde, F., 2006. Effect of applied stresses on alkali–silica reaction-induced expansions. Cement and Concrete Research 36, 912–920.

Multon, S., Toutlemonde, F., 2010. Effect of moisture conditions and transfer on alkali silica reaction damaged structures. Cement and Concrete Research 40, 924–934.

Poyet, S. 2003. Etude de la dégradation des ouvrages en beéton atteints par la reéaction alcali-silice: Approche expeérimentale et modeélisation numeérique multi-eéchelles dans un environnement hydro-chemo-mécanique variable. Ph.D. thesis, Université de Marne de Vallée.

Poyet, S., Sellier, A., Capra, B., Thèvenin-Foray, G., Torrenti, J.-M., Tournier-Cognon, H., Bourdarot, E., 2006. Influence of water on alkali–silica reaction. experimental study and numerical simulation. Journal of Materials in Civil Engineering 18 (4), 588–596.

Raphael, S., Sarkar, S.L., Aitcin, P.-C. 1989. Alkali–aggregate reactivity – is it always harmful? in: Alkali–aggregate reaction: 8th international conference Kyoto, 809–814.

Saouma, V., Perotti, L., 2006. Constitutive model for alkali–aggregate reactions. ACI Material Journal 103 (194-202).

Saouma, V., Perotti, L., Shimpo, T., 2007. Stress analysis of concrete structures subjected to alkali–aggregate reactions. ACI Structural Journal 104 (5), 532–541.

Ulm, F., Coussy, O., Kefei, L., Larive, C., 2000. Thermo–chemo-mechanics of ASR expansion in concrete structures. ASCE Journal of Engineering Mechanics 126 (3), 233–242.

Van Genuchten, M., 1980. A closed-form equation for predicting the hydraulic conductivity of unsaturated soils. Soil Science Society of America Journal 44, 892–898.